A GENERAL METHOD FOR THE DETERMINATION OF THE LOCAL ORTHOTROPIC DIRECTIONS OF HETEROGENEOUS MATERIALS: APPLICATION TO BONE STRUCTURES USING µCT IMAGES

CHRISTOPHE CLUZEL AND RACHELE ALLENA

To assess the degree (i.e., isotropy, transverse isotropy, or orthotropy) and the directions of anisotropy of a three-dimensional structure, information about its mesostructure is necessary. Usually, a topological analysis of computed tomography or microcomputed tomography images is performed and requires an interpretation of the constitutive elements of the three-dimensional structure, which may lead to a simplistic description of the geometry. In this paper we propose an alternative technique based on a geometric tensor and we use it to analyze 38 representative elementary volumes extracted from 24 specimens of cortical bone in a human femur whose geometries have been reconstructed via microcomputed tomography images.

1. Introduction

Computed tomography (CT) and microcomputed tomography (µCT) are powerful imaging tools allowing the visualization of three-dimensional (3D) geometries which can be used to simulate the global and personalized response of the mechanical structure [Rémond et al. 2016]. If such geometries are constituted of heterogeneous materials like bone or composites [Placidi et al. 2017; Giorgio et al. 2017], one needs to describe their constitutive behavior as a function of the local systems of anisotropy. Then, additional information is required at the scale of their mesostructure to identify the anisotropic field.

Cortical bone is constituted of several elements oriented in space leading to a very significant anisotropy at different levels, from the nanoscale (i.e., collagen fibers) to the mesoscale (i.e., osteons) [Rho et al. 1998]. As a consequence, the elastic behavior at the macroscale is highly anisotropic and more specifically orthotropic as has been quantified in [Rho 1996; Bernard et al. 2013].

The identification of the directions of orthotropy may be straightforward and given by the direct observation of the Haversian canals. For instance, in [Heřt

et al. 1994; Petrtýl et al. 1996], the canals are previously ink-soaked and then developed by successive polishing. A similar technique has also been adopted by Báča et al. [2007] to describe the directions of the canals on the bone surface.

Alternatively, a topological analysis of CT or μCT images can be employed to identify the degree (i.e., isotropy, transverse isotropy, or orthotropy) and the main directions of anisotropy after a 3D skeletonization as in [Pothuaud et al. 2000] or a 3D finite element (FE) simulation as in [Nazemi et al. 2016], both applied on trabecular bone. Nonetheless, such an approach requires a complex interpretation of the constitutive elements of the 3D structure. Therefore, in this paper we propose an alternative technique based on a geometric tensor and we use it to analyze a series of representative elementary volumes (REVs) extracted from cortical bone specimens and whose 3D geometries are obtained via μCT images. Assuming an orthotropic elastic behavior for the cortical bone, the average directions of the mesostructure are computed.

In the following sections we describe the experimental approach used to identify the main directions of orthotropy of the cortical bone mesostructure. This includes the specimen extraction (Section 2.1.1), the μCT imaging (Section 2.1.2), and the computation of the geometrical tensor associated with the femur mesostructure (Section 2.1.3). In Section 3, we first show the consistency of the technique to identify the directions of orthotropy through simple geometric configurations (Section 3.1) and second we apply our approach on the bone specimens (Section 3.2). Finally, in Section 4, the results are discussed and some limitations and perspectives of the work are considered.

2. Material and methods

2.1. *Experimental analysis of the orthotropic field.*

2.1.1. *CT-scanning and specimen extraction.* A left human male femur (91 years old) was collected and frozen at $-20\,°C$ in a plastic bag. Once defrosted, the femur was cleaned by a clinician to remove soft tissues around it and dried with ethanol.

A total of 24 specimens S_i, with i from 1 to 24, were extracted at different regions of the proximal side of the femur as follows (Figure 1):

- 3 along the upper anterior diaphysis (AD) (S_1 to S_3),
- 2 in the greater trochanter (GT) (S_4 and S_5),
- 4 around and on top of the lesser trochanter (LT) (S_6 to S_9),
- 3 along the femoral neck (N) (S_{10} to S_{12}),
- 2 in the femoral head (H) (S_{13} and S_{14}),
- 4 in the upper posterior diaphysis (PD) (S_{15} to S_{18}), and
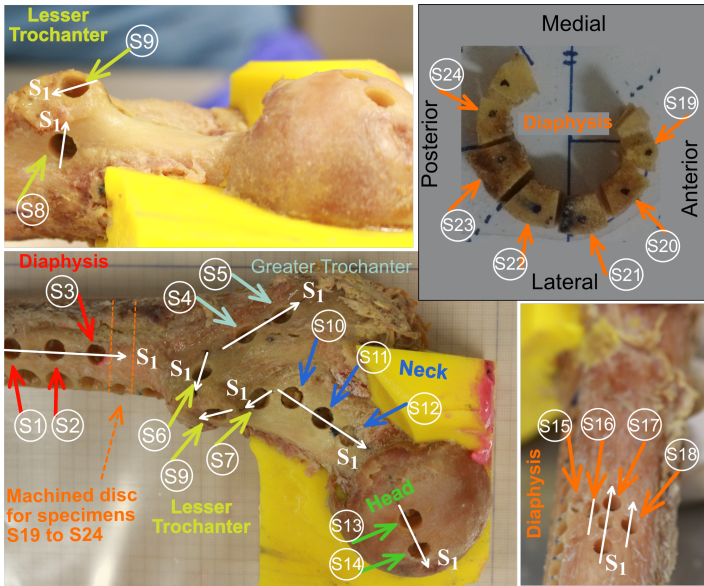- 6 around the diaphysis (D) (S_{19} to S_{24}).

Figure 1. Extraction and position of the 24 specimens from the human left femur.

Diamond-tipped drills were used to machine specimens S_1 to S_{18}, which have a cylindrical shape with diameter 6 mm and height equal to the thickness of the cortical bone. Specimens S_{19} to S_{24} were manually cut and show a trapezoidal shape. During the cutting, water was used in order to reduce both friction and temperature rise. Before the extraction, an easily identifiable mark in the direction S_1 has been carved on the external surface of each specimen in order to orient it with respect to the femur (Figures 1 and 2). The direction S_1 is used to locate each specimen in the femur when the 3D microstructure is reconstructed from μCT images. Thus, it could be any direction. Here, for the sake of simplicity, we have
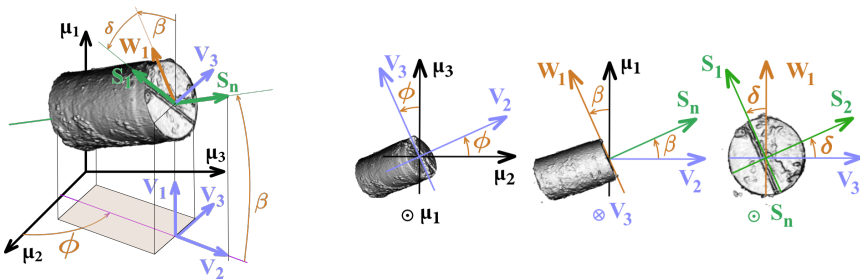

Figure 2. Position of a specimen with respect to the μCT system of coordinates R_μ.
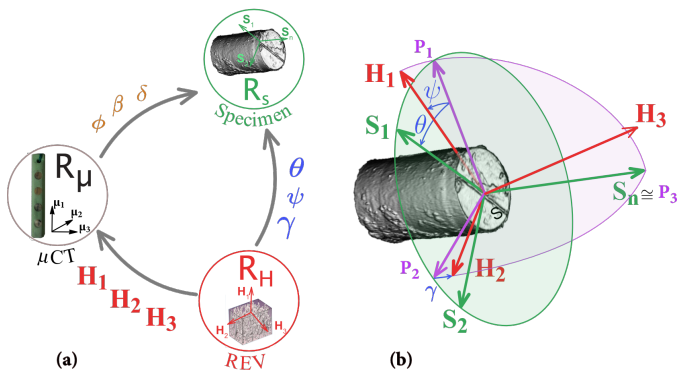
Figure 3. (a) Main steps to acquire the directions of orthotropy of the Haversian canals. (b) Angles defining the projection of R_H on the external surface of the specimen.

decided to let it coincide with the middle line of the femur in each region of interest (Figure 1). Specimens were immersed in a solution of zinc iodide for 24 hours to stain the Haversian canals inside the osteons.

2.1.2. *μCT imaging.* The specimens were placed on a shelf trying to align the direction S_1 with the vertical axis μ_1 of the μCT scanner in the best possible way (Figure 3b). They were scanned using a μCT scanner (Scanco Medical XtremeCT with voxel size 7.4 μm). It consisted of a microfocus X-ray source, a rotating specimen holder, and a detector system, with a 2048×2048 pixel CCDD camera. The images were acquired using the following protocol: 90 kVp, 155 μA, 0.5 mm aluminum filter, and integration time 200 ms per slice.

After acquisition, a stack of about 800 cross-sectional images stored in DICOM format was obtained and the 3D reconstruction was made using software from FEI (Hillsboro, Oregon, USA). First, we built the 3D volume of the specimens in order to compute the outward normal vector S_n to its external surface (Figure 3b). Second, by defining a specific threshold and by extracting one or more representative elementary volumes (REVs) for each specimen, we were able to obtain the 3D network of the Haversian canals. It is worth noting that an REV includes a sufficient number of osteons (i.e., at least 10, which corresponds to 3 to 4 osteons per side) and does not present any porosity which could trigger artifacts. In both cases (whole specimen and REV), the final 3D geometry was stored as an STL file constituted of a large number of facets N_f ($150000 < N_f < 200000$) providing a uniform and smooth surface.

2.1.3. *Identification of the main directions of the Haversian canals.* In this section we detail the successive steps used to acquire the main directions of orthotropy

associated with the Haversian canals (Figure 3a). Each system of reference used in this section is a direct orthonormal system of coordinates.

First, each specimen S_i is defined by its proper system of reference $R_S = \{S_1, S_2, S_n\}$, where the subscript S stands for specimen, S_1 and S_n were previously defined (Section 2.1.1), and S_2 is obtained via a vector product between S_1 and S_n (Figure 3b). In order to determine the position of the specimen with respect to the μCT system of reference $R_\mu = \{\mu_1, \mu_2, \mu_3\}$ (the subscript μ stands for μCT), three angles are measured between R_s and R_μ: ϕ, β, and δ (Appendix A1).

Second, once an REV is extracted from a specimen and using the geometrical information included in the STL files previously obtained (Section 2.1.2), the system of reference $R_H = \{H_1, H_2, H_3\}$ (the subscript H stands for Haversian canals) can be computed. To do so, rather than performing a topological analysis [Boyle and Kim 2011] of the REV surface mesh which would require an approximation of each Haversian canal by a regular geometry, we propose an approach which only takes into account the external surface of each Haversian canal while maintaining the precision, as demonstrated via simple illustrative examples in Section 3.1.

Each facet of the REV surface mesh is identified by its proper outward normal vector n_j. Since for each REV the mesh facets have mostly the same area and their total number N_f is high, no weighting has been applied. The product $n_j n_j^T$ enables one to obtain a tensorial form of n_j, which includes more information than the vector itself (i.e., eigenvalues and eigenvectors). Then, by summing all these tensors, the global tensor G can be computed as

$$G = \sum_{j=1}^{N_f} n_j n_j^T.$$
(1)

To quantify the morphology and the geometrical effects, we use the normalized eigenvalues $0 \leq \lambda_k \leq 3$, with $k \in [1, 2, 3]$, of G, which are obtained from the eigenvalues $\lambda_{10} \leq \lambda_{20} \leq \lambda_{30}$ as

$$\lambda_k = \frac{3\lambda_{k0}}{\lambda_{10} + \lambda_{20} + \lambda_{30}}.$$
(2)

For each normalized eigenvalue λ_k, the associated eigenvector H_k can be calculated.

Finally, the projection of R_H on the external surface of the specimen is computed to obtain the system of reference $R_P = \{P_1, P_2, P_3\}$, where the subscript P stands for projection (Appendix A2). The vectors P_1, P_2, and P_3 are the projections of H_1, H_2, and H_3, respectively (Figure 3b). Then, the position of R_H for each REV with respect to R_S can be found through three angles: ψ, γ, and θ (Figures 3b and 4). The vector P_1 will be directly compared to the corresponding numerical vector, which is obtained as described in the following sections.
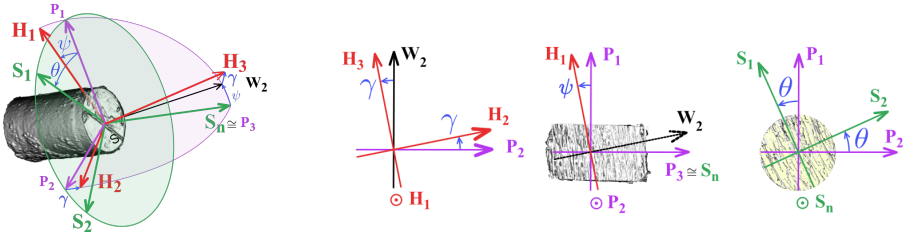
Figure 4. Angles defining the projection of R_H on the external surface of the specimen (W_2 is an intermediate unit vector).

3. Results

3.1. *Validation of the technique to identify the directions of orthotropy.*

To validate and illustrate our approach presented in Section 2.1.3, five simple examples, whose average direction V is known, are proposed as shown in Figure 5.

It has to be noticed that the cutting sections of the tubes are not proper surfaces of the tubes themselves but rather fictive ones obtained through the REV extraction. Therefore, for configurations (a) to (d), the upper and lower cutting planes are not taken into account. However, for the sake of practicality, for configuration (e) the extremities are included in the analysis.

For each configuration, the tubes are characterized by their direction V_{t0} (t being the number of the tube in the specific configuration and going from 1 to N_t, the total number of tubes), which is defined in a spherical system of coordinates as $V_{t0} = \{\cos\alpha_t \cos\gamma_t, \cos\alpha_t \sin\gamma_t, \sin\alpha_t\}$.

The average direction V of a configuration is then defined as

$$V = \frac{\sum_{l=1}^{N_t} V_{t0}}{\left\| \sum_{l=1}^{N_t} V_{t0} \right\|} \tag{3}$$
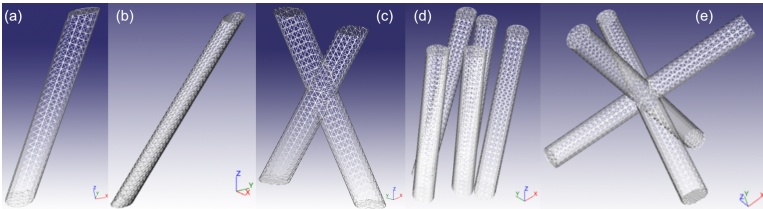

Figure 5. Simple examples to illustrate our approach to compute the geometric tensor G. (a) Single tube with circular section. (b) Single tube with elliptical section. (c) Two crossed tubes. (d) Five noncrossed and randomly oriented tubes with circular section. (e) Three orthogonally crossed tubes.

	(a)	(b)	(c)	(d)	(e)
α_t/γ_t	60°/30°	60°/30°	60°/90° 60°/−90°	50°/20° 55°/25° 60°/30° 65°/35° 70°/40°	0°/0° 0°/90° 90°/0°
V	0.433 0.250 0.866	0.433 0.250 0.866	0 0 1	0.437 0.237 0.868	
λ_1 λ_2 λ_3	0.010 1.480 1.510	0.000 0.990 2.010	0.320 0.930 1.750	0.03 1.420 1.540	0.998 1.001 1.001
H_1	0.432 0.251 0.866	0.433 0.250 0.866	−0.001 0.001 1.000	0.408 0.240 0.881	0.577 0.577 0.577
H_2	0.517 0.718 −0.466	−0.501 0.865 0.001	−0.013 0.999 −0.001	0.598 0.659 −0.456	−0.305 −0.503 0.808
Anisotropy mode	TI	O	O	TI	I

Table 1. Overall results for each configuration (a) to (e) (TI = transverse isotropy, O = orthotropy, and I = isotropy).

with $\|\cdot\|$ the Euclidean norm of a vector. The results associated with each configuration are reported in Table 1. The direction V can be alternatively computed using the approach presented in Section 2.1.3. In fact, the first eigenvector H_1 of the geometrical tensor G corresponds to V. It is interesting to notice that an eigenvector H_k (k going from 1 to 3) is correctly computed only if the associated eigenvalue λ_k is notably different from the other two. Thus, the direction V is properly estimated by the proposed approach for cases (a) to (d). However, for case (e), the eigenvalues λ_k of G being identical and close to 1, the overall geometry is isotropic and the eigenvectors do not provide any further information. Similarly, the eigenvector H_2 is indicative only if the eigenvalues λ_2 and λ_3 are different. This is not the case for configurations (a) and (d) where there is not a preferential transversal direction (i.e., transverse isotropy). Finally, for cases (b) and (c), the eigenvector H_2 clearly shows the geometrical orthotropy.

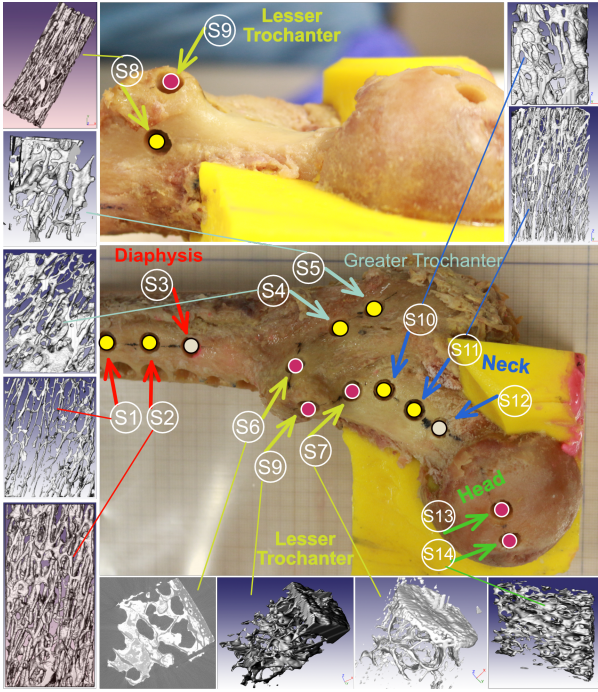The consistency of our technique has then been shown, and we can now apply it to the cortical bone.

Figure 6. 3D reconstruction of the Haversian canals network for the REVs extracted from specimens S_1, S_2, S_4, S_5, S_8, S_{10}, and S_{11} (yellow circles). For the other specimens (pink or gray circles), the reconstruction was not possible due to the very thin cortical thickness or some technical issues.

3.2. *Measurement of the directions of orthotropy.*

For each of the 24 specimens the 3D geometry was reconstructed and its position with respect to the μCT system of coordinates R_μ was identified. In order to obtain the main direction $\boldsymbol{H}_1$ of the Haversian canals, at least one REV for each specimen was extracted where only Haversian canals (i.e., no large porosities) could be observed. Nevertheless, for some specimens (i.e., S_6, S_7, S_9, S_{13}, and S_{14}) only a few Haversian canals (i.e., fewer than five) could be segmented due to the very thin thickness of the cortical domain. Then, the orthotropic system of coordinates R_H could not be computed, but we rather estimated the eigenvectors $\boldsymbol{H}_k$ of the geometric tensor $\boldsymbol{G}$ associated with the spongy trabeculae. Additionally, specimens S_3, S_6, and S_{12} could not be retrieved due to some technical issues. In Figure 6, the REVs for specimens S_1, S_2, S_4, S_5, S_8, S_{10}, and S_{11} are presented. In summary, we distinguish between the specimens with a cortical thickness h_C greater (19, named cortical specimens) and less (5, named trabecular specimens) than 0.5 mm. In the following sections, for each specimen we identify the eigenvalues (λ_1, λ_2, λ_3) of the geometric tensor $\boldsymbol{G}$,

S_i	REV	region	s.t.	λ_1	λ_2	λ_3	θ °±1	ψ °±1	γ °±1	h_c mm±0.4	a.m.
S_1	$S_{1,1}$	AD	C	0.39	0.93	1.67	−20.1	11.2	−3.8		O
S_2	$S_{2,1}$	AD	C	0.46	1.12	1.42	−9.9	2.0	−35.5	4.1	O/TI
S_3	$S_{3,1}$	AD	C								LD
S_4	$S_{4,1}$	GT	C	0.42	1.06	1.52	31.3	1.1	0.9	0.8	O
S_5	$S_{5,1}$	GT	C	0.38	0.76	1.86	20.5	3.0	10.4	0.8	O
S_6	$S_{6,1}$	LT	T							0.5	NVM
S_7	$S_{7,1}$	LT	T	0.43	0.72	1.80	33.0	2.9	5.7	0.4	O
S_8	$S_{8,1}$	LT	C	0.35	1.01	1.64	87.5	0.2	−3.5	2.5	O
S_9	$S_{9,1}$	LT	T	0.62	0.99	1.39	70.8	9.8	83.9	0.5	O
S_{10}	$S_{10,1}$	N	C	0.37	0.74	1.90	20.5	7.3	3.9	0.7	O
S_{11}	$S_{11,1}$	N	C	0.37	1.14	1.48	−2.3	5.2	−0.2		O
S_{12}	$S_{12,1}$	N	C								LD
S_{13}	$S_{13,1}$	H	T	0.43	1.04	1.53	−96.1	80.5	−69.1		O
S_{14}	$S_{14,1}$	H	T	0.43	1.08	1.49	−89.2	79.7	−60.9	0.5	O
S_{15}	$S_{15,1}$	PD	C	0.76	1.11	1.14	−7.5	7.9	−53.2	5.3	TI
S_{16}	$S_{16,1}$	PD	C	0.63	1.10	1.28	−4.2	6.2	87.4	5.7	O/TI
S_{17}	$S_{17,1}$	PD	C	0.58	1.11	1.31	10.6	4.4	−89.1	6.1	O/TI
S_{18}	$S_{18,1}$	PD	C	0.39	1.20	1.40	9.6	1.7	−28.3	6.0	O/TI

Table 2. Overall results for specimens S_1 to S_{18}. Under s.t. (specimen type): C = cortical, T = trabecular. Under a.m. (anisotropy mode): TI = transverse isotropy, O = orthotropy, I = isotropy, LD = lost data, NVM = no visible mark.

the angles θ, ψ, and γ, and the cortical thickness h_C. In Tables 2 and 3 all the results are reported. For the angles, the uncertainty of 1° is due to the manual measurement. For the cortical thickness, an uncertainty of 0.4 mm corresponds to the largest transition region between the cortical and the spongy bone.

3.2.1. *Cortical specimens.* Although in reality there is no sharp transition between isotropy (I), transverse isotropy (TI), and orthotropy (O), here, in order to classify the degree of anisotropy for each specimen S_i, we have defined the intervals

- for I $|\lambda_i - \lambda_j| \leq 0.05$,
- between I and TI $0.05 < |\lambda_i - \lambda_j| < 0.37$,
- for TI with respect to H_1 $|\lambda_2 - \lambda_1| \geq 0.37$ and $|\lambda_3 - \lambda_2| \leq 0.05$,
- between TI and O $|\lambda_2 - \lambda_1| \geq 0.37$ and $0.05 < |\lambda_3 - \lambda_2| < 0.37$, and
- for O $|\lambda_i - \lambda_j| \geq 0.37$,

where i, $j \in \{1, 2, 3\}$ and $i \neq j$.

Overall, for each cortical specimen, λ_1 is much smaller than λ_2 and, more specifically, we found that specimens S_2, S_{15}, S_{16}, S_{17}, and S_{18} show a transverse isotropy.

S_i	REV	χ $°\pm1$	region	s.t.	λ_1	λ_2	λ_3	θ $°\pm1$	ψ $°\pm1$	γ $°\pm1$	a.m.
S_{19}	$S_{19,1}$	−11.3	D	C	0.62	1.06	1.30	8.4	1.8	−2.5	O/TI
	$S_{19,2}$	−4.6	D	C	0.76	1.04	1.20	2.1	−2.1	−16.3	TI/I
	$S_{19,3}$	5.4	D	C	0.68	0.97	1.35	3.6	1.6	−4.7	O
S_{20}	$S_{20,1}$	33.4	D	C	0.64	1.03	1.33	16.3	7.3	12.0	O
	$S_{20,2}$	42.4	D	C	0.68	1.03	1.29	19.4	4.4	−7.5	O/TI
	$S_{20,3}$	51.8	D	C	0.59	1.10	1.31	16.8	1.8	−26.3	O/TI
S_{21}	$S_{21,1}$	70.0	D	C	0.62	1.08	1.30	11.7	−0.6	−36.1	O/TI
	$S_{21,2}$	80.3	D	C	0.63	1.10	1.27	10.2	−1.6	−34.2	O/TI
	$S_{21,3}$	87.7	D	C	0.53	1.21	1.26	8.6	−1.9	−71.3	TI
S_{22}	$S_{22,1}$	100.9	D	C	0.62	1.05	1.33	9.3	0.6	−26.1	O/TI
	$S_{22,2}$	118.2	D	C	0.61	1.13	1.26	9.5	−0.4	−5.6	O/TI
	$S_{22,3}$	122.3	D	C	0.51	1.05	1.44	9.2	1.1	−18.9	O
	$S_{22,4}$	126.9	D	C	0.68	1.05	1.27	18.0	−1.1	−17.9	O/TI
	$S_{22,5}$	130.0	D	C	0.74	1.05	1.21	16.6	−1.1	−5.1	TI/I
S_{23}	$S_{23,1}$	147.2	D	C	0.65	1.07	1.28	4.7	−0.7	−13.1	O/TI
	$S_{23,2}$	160.2	D	C	0.68	0.99	1.32	1.3	0.6	−4.8	O/TI
	$S_{23,3}$	171.1	D	C	0.71	1.01	1.28	−7.9	2.7	−7.9	O/TI
S_{24}	$S_{24,1}$	181.0	D	C	0.79	1.09	1.12	−23.1	−1.7	−17.2	TI
	$S_{24,2}$	187.1	D	C	0.67	0.99	1.34	−35.9	−5.7	−1.4	O
	$S_{24,3}$	197.6	D	C	0.68	1.06	1.26	−28.6	−16.1	−22.9	O/TI

Table 3. Overall results for specimens S_{19} to S_{24}. Under s.t. (specimen type): C = cortical. Under a.m. (anisotropy mode): TI = transverse isotropy, O = orthotropy, I = isotropy.

Then, in these cases, the angle γ, which generally provides the circumferential direction, is not relevant since $\lambda_2 \approx \lambda_3$. The remaining cortical specimens (i.e., S_1, S_4, S_5, S_8, S_{10}, and S_{11}) are orthotropic. Around the diaphysis (i.e., from S_{19} to S_{24}), some REVs clearly show an orthotropic behavior, whereas others are between orthotropy and transverse isotropy (Table 3).

It is interesting to focus on the specimens in the AD (S_1 and S_2), in the PD (from S_{15} to S_{18}), and around the diaphysis (from S_{19} to S_{24}) for which $h_c > 0.5$ and the Haversian canals are uniformly oriented. We found that the angle θ between the drawn mark $\boldsymbol{S}_1$ on each specimen and $\boldsymbol{P}_1$, the projection of the principal direction of the Haversian canals $\boldsymbol{H}_1$ on the external surface of the femur, varies between $-35.86°$ for $S_{24,2}$ and $19.44°$ for $S_{20,2}$.

We analyzed the evolution of θ along the radial direction (Figure 7). To do so, we split the reconstructed S_1 specimen into seven successive slices with a spacing of 0.5 mm (Figure 7) and we found θ equal to (a) $-43°$, (b) $-22°$, (c) $-15°$, (d)

Image	λ_1	λ_2	λ_3	θ (°)
Figure 7a	0.39	0.55	1.09	-42.7
Figure 7b	0.44	0.99	1.56	-21.9
Figure 7c	0.40	0.98	1.61	-15.0
Figure 7d	0.37	1.15	1.48	-16.1
Figure 7e	0.39	1.22	1.39	-16.6
Figure 7f	0.44	1.15	1.40	-17.6
Figure 7g	0.44	1.18	1.38	-14.9

Table 4. Results for the extracted slices from specimen S_1.

$-16°$, (e) $-17°$, (f) $-18°$, and (g) $-15°$. If we consider that in the outermost slices (parts (a) and (b) of Figure 7) the presence of the external surface distorts the final outcome, one may conclude that θ does not change significantly when going from the outer to the inner cortical domain. The computed angles are reported in Table 4.
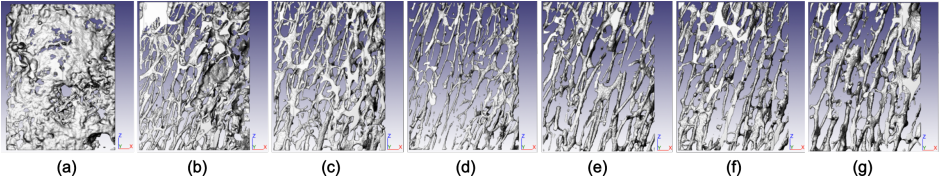

Figure 7. Successive slices from the exterior (a) to the interior (g) of an REV of specimen S_1.
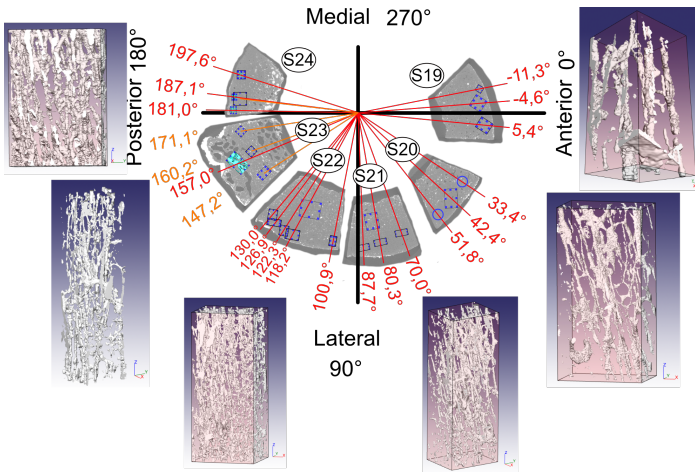

Figure 8. Specimens S_{19} to S_{24} with the relative circumferential position χ and some of the extracted REVs.
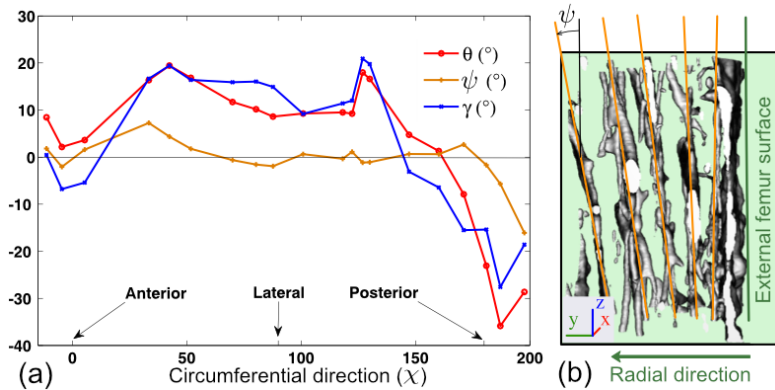
Figure 9. (a) Evolution of θ, ψ, and γ with respect to the circumferential position χ of the REVs in specimens S_{19} to S_{24}. (b) Orientation of ψ close to the external surface of the femur.

For specimens S_{19} to S_{24}, twenty REVs were extracted, whose position around the diaphysis circumference is defined by the angle χ, varying between $-11.3°$ and $197.6°$ (Figure 8 and Table 3). In Figure 9a, the evolutions of the angles θ (red line), ψ (brown line), and γ (blue line) around the upper diaphysis (i.e., from the anterior to the posterior region passing by the lateral region) are shown. We can notice that θ and γ vary as functions of the circumferential coordinate χ, whereas ψ does not change significantly.

Finally, we investigated the variation of ψ, the angle between $\boldsymbol{P}_1$ and $\boldsymbol{H}_1$, across the cortical thickness along the radial direction for the specimen S_1. We found that, closer to the outer surface, the Haversian canals are nearly parallel to the surface (Figure 9b).

3.2.2. *Trabecular specimens.* As mentioned earlier, for some specimens (S_6, S_7, S_9, S_{13}, and S_{14}) the cortical thickness is very thin. Thus, it is difficult to extract an REV with isolated Haversian canals and identify the average direction $\boldsymbol{H}_1$.

Although in the present work we focus on the orthotropy of the cortical bone, it is interesting to quantify the geometric tensor $\boldsymbol{G}$ and the associated variables for such specimens (Table 2). To do so, the parameters used for the reconstruction of the 3D geometries from the μCT images have been adapted in order to detect the trabeculae and larger REVs have been extracted.

Some remarks can be drawn. For specimens S_{13} and S_{14} extracted in the head, the angle ψ is equal to $80.5°$ and $79.7°$, respectively. This means that the spongy trabeculae are mainly oriented perpendicular to the outer surface of the femur. On the contrary, for specimens S_7 and S_9 extracted in the neck, ψ is found equal to $2.9°$ and $9.8°$, respectively, which implies that the trabeculae are almost parallel to

the external femoral surface (Table 2). Such outcomes are in agreement with the literature and more specifically with the works of Jacobs et al. [1995] and Tsubota et al. [2009].

4. Discussion

Our approach is based on experimental data and more specifically on μCT images of the Haversian network, which provide the same trends found in [Petrtýl et al. 1996; Wirtz et al. 2003; Báča et al. 2007]. We have defined a geometric tensor G, via the outward normal vectors to the facets of an REV, and we have computed its eigenvalues and eigenvectors to estimate the degree and the directions of orthotropy, respectively.

Despite the interesting results, such a technique shows few main drawbacks. First, the position of each specimen with respect to the μCT system of coordinates R_μ needs to be carefully retrieved in order to obtain consistent results. Second, it is a discrete approach since the measurements are obtained via a series of specimens in specific regions of the 3D structure. In order to circumvent this issue, we propose in a further work a numerical technique based on diffusion equations and on the experimental data obtained in this paper. This approach will allow us to get a continuum description of the field of orthotropic directions in a 3D structure such a femur.

Appendix

A1. *Position of R_S with respect to R_μ.* As explained in Section 2.1.3, it is necessary to determine the position of a specimen S_i with respect to the μCT. Each specimen is identified by the mark S_1 and the outward normal vector S_n, which constitute with S_2 the system of coordinates $R_S = \{S_1, S_2, S_n\}$. During the image acquisition, the position of a specimen with respect to the μCT system of coordinates $R_\mu = \{\mu_1, \mu_2, \mu_3\}$ is defined by three angles (Figure 2):

- ϕ, the angle between μ_2 and V_2,
- β, the angle between V_2 and S_n, and
- δ, the angle between W_1 and S_1,

where $R_v = \{V_1, V_2, V_3\}$ is an intermediate system of reference obtained by projecting the specimen on the plane (μ_2, μ_3). Then, $V_1 = \mu_1$, V_2 is the normalized projection of S_n on the plane (μ_2, μ_3), and V_3 is the cross product between V_1 and V_2. Finally, the vector W_1 is the normalized projection of V_1 on the specimen external surface.

A2. *Projection of R_H on the external surface of a specimen.* As described in Section 2.1.3, it is necessary to identify the position of the Haversian canals with

respect to the specimen. When an REV is extracted from a specimen, the system of orthotropic coordinates $R_H = \{H_1, H_2, H_3\}$ of the Haversian canals can be determined. The projection of R_H on the external surface of the specimen is computed and the system of reference R_P is obtained. Then, three angles define the position of R_H with respect to R_S (Figure 4):

- θ, the angle between P_1 and S_1, expressed as

$$\theta = -\arcsin(P_1^T S_2), \tag{4}$$

- ψ, the angle between H_1 and P_1, which reads

$$\psi = -\arcsin(S_n^T H_1), \tag{5}$$

  and

- γ, the angle between H_2 and P_2, defined as

$$\gamma = -\arcsin(P_2^T H_3), \tag{6}$$

where $(c^T d)$ indicates the dot product, the superscript T the transpose of a vector, and

$$P_2 = \frac{H_1 \wedge S_n}{\|H_1 \wedge Sn\|}, \tag{7}$$

$$P_1 = \frac{S_n \wedge P_2}{\|S_n \wedge P_2\|} \tag{8}$$

with $(c \wedge d)$ the vector product. It is worth noting that in (4), (5), and (6), rather than simply computing the arc cosine between the two involved vectors, the arc sine is used in order to detect the sign of the angle of interest.

Acknowledgements

References

[Báča et al. 2007] V. Báča, D. Kachlík, Z. Horák, and J. Stingl, "The course of osteons in the compact bone of the human proximal femur with clinical and biomechanical significance", *Surg. Radiol. Anat.* **29**:3 (2007), 201–207.

[Bernard et al. 2013] S. Bernard, Q. Grimal, and P. Laugier, "Accurate measurement of cortical bone elasticity tensor with resonant ultrasound spectroscopy", *J. Mech. Behav. Biomed.* **18** (2013), 12–19.

[Boyle and Kim 2011] C. Boyle and I. Y. Kim, "Three-dimensional micro-level computational study of Wolff's law via trabecular bone remodeling in the human proximal femur using design space topology optimization", *J. Biomech.* **44**:5 (2011), 935–942.

[Giorgio et al. 2017] I. Giorgio, U. Andreaus, F. dell'Isola, and T. Lekszycki, "Viscous second gradient porous materials for bones reconstructed with bio-resorbable grafts", *Extreme Mech. Lett.* **13** (2017), 141–147.

[Heřt et al. 1994] J. Heřt, P. Fiala, and M. Petrtýl, "Osteon orientation of the diaphysis of the long bones in man", *Bone* **15**:3 (1994), 269–277.

[Jacobs et al. 1995] C. R. Jacobs, M. E. Levenston, G. S. Beaupré, J. C. Simo, and D. R. Carter, "Numerical instabilities in bone remodeling simulations: the advantages of a node-based finite element approach", *J. Biomech.* **28**:4 (1995), 449–451.

[Nazemi et al. 2016] S. M. Nazemi, D. M. L. Cooper, and J. D. Johnston, "Quantifying trabecular bone material anisotropy and orientation using low resolution clinical CT images: a feasibility study", *Med. Eng. Phys.* **38**:9 (2016), 978–987.

[Petrtýl et al. 1996] M. Petrtýl, J. Heřt, and P. Fiala, "Spatial organization of the haversian bone in man", *J. Biomech.* **29**:2 (1996), 161–169.

[Placidi et al. 2017] L. Placidi, U. Andreaus, and I. Giorgio, "Identification of two-dimensional pantographic structure via a linear D4 orthotropic second gradient elastic model", *J. Eng. Math.* **103** (2017), 1–21.

[Pothuaud et al. 2000] L. Pothuaud, P. Porion, E. Lespessailles, C. L. Benhamou, and P. Levitz, "A new method for three-dimensional skeleton graph analysis of porous media: application to trabecular bone microarchitecture", *J. Microsc.* **199**:2 (2000), 149–161.

[Rémond et al. 2016] Y. Rémond, S. Ahzi, M. Baniassadi, and H. Garmestani, *Applied RVE reconstruction and homogenization of heterogeneous materials*, Wiley, 2016.

[Rho 1996] J.-Y. Rho, "An ultrasonic method for measuring the elastic properties of human tibial cortical and cancellous bone", *Ultrasonics* **34**:8 (1996), 777–783.

[Rho et al. 1998] J.-Y. Rho, L. Kuhn-Spearing, and P. Zioupos, "Mechanical properties and the hierarchical structure of bone", *Med. Eng. Phys.* **20**:2 (1998), 92–102.

[Tsubota et al. 2009] K.-i. Tsubota, Y. Suzuki, T. Yamada, M. Hojo, A. Makinouchi, and T. Adachi, "Computer simulation of trabecular remodeling in human proximal femur using large-scale voxel FE models: approach to understanding Wolff's law", *J. Biomech.* **42**:8 (2009), 1088–1094.

[Wirtz et al. 2003] D. C. Wirtz, T. Pandorf, F. Portheine, K. Radermacher, N. Schiffers, A. Prescher, D. Weichert, and F. U. Niethard, "Concept and development of an orthotropic FE model of the proximal femur", *J. Biomech.* **36**:2 (2003), 289–293.

CHRISTOPHE CLUZEL: cluzel@lmt.ens-cachan.fr
Laboratoire de Mécanique et Technologie, Ecole Normale Supérieure Paris Saclay, Cachan, France

RACHELE ALLENA: rachele.allena@ensam.eu
Institute de Biomécanique Humaine George Charpak, Arts et Métiers ParisTech, Paris, France